PAPER

Tomography of fast-ion velocity-space distributions from synthetic CTS and FIDA measurements

To cite this article: M. Salewski *et al* 2012 *Nucl. Fusion* **52** 103008

IOP Publishing and International Atomic Energy Agency Nuclear Fusion

Nucl. Fusion **52** (2012) 103008 (11pp) doi:10.1088/0029-5515/52/10/103008

Tomography of fast-ion velocity-space distributions from synthetic CTS and FIDA measurements

M. Salewski[1], B. Geiger[2], S.K. Nielsen[1], H. Bindslev[3], M. García-Muñoz[2], W.W. Heidbrink[4], S.B. Korsholm[1], F. Leipold[1], F. Meo[1], P.K. Michelsen[1], D. Moseev[2,5], M. Stejner[1], G. Tardini[2] and the ASDEX Upgrade team[2]

[1] Association Euratom-DTU, Technical University of Denmark, Department of Physics, DTU Risø Campus, DK-4000 Roskilde, Denmark
[2] Association Euratom-Max-Planck-Institut für Plasmaphysik, D-85748 Garching, Germany
[3] Faculty of Sciences and Technology, Aarhus University, DK-8000 Aarhus C, Denmark
[4] Department of Physics and Astronomy, University of California, Irvine, CA 92697, USA
[5] Association Euratom-FOM Institute DIFFER, 3430 BE Nieuwegein, The Netherlands

E-mail: msal@fysik.dtu.dk

Received 10 May 2012, accepted for publication 1 August 2012
Published 21 August 2012
Online at stacks.iop.org/NF/52/103008

Abstract
We compute tomographies of 2D fast-ion velocity distribution functions from synthetic collective Thomson scattering (CTS) and fast-ion D_α (FIDA) 1D measurements using a new reconstruction prescription. Contradicting conventional wisdom we demonstrate that one single 1D CTS or FIDA view suffices to compute accurate tomographies of arbitrary 2D functions under idealized conditions. Under simulated experimental conditions, single-view tomographies do not resemble the original fast-ion velocity distribution functions but nevertheless show their coarsest features. For CTS or FIDA systems with many simultaneous views on the same measurement volume, the resemblance improves with the number of available views, even if the resolution in each view is varied inversely proportional to the number of views, so that the total number of measurements in all views is the same. With a realistic four-view system, tomographies of a beam ion velocity distribution function at ASDEX Upgrade reproduce the general shape of the function and the location of the maxima at full and half injection energy of the beam ions. By applying our method to real many-view CTS or FIDA measurements, one could determine tomographies of 2D fast-ion velocity distribution functions experimentally.

(Some figures may appear in colour only in the online journal)

1. Introduction

Fast ions play a key role in high performance plasmas: they mediate energy from external heating sources or fusion reactions to the bulk plasma and so maintain the high temperatures typical for fusion-relevant plasmas. The fast-ion orbits can be perturbed by fluctuations in the plasma, and the ions can then be prematurely ejected from the plasma, leading to undesired local heating of the first wall instead of plasma heating. Several types of modes selectively deplete or reorganize fast ions in particular velocity-space regions, for example sawteeth [1–3], Alfvén eigenmodes [4–6] and neoclassical tearing modes [7]. Turbulence also ejects ions selectively depending on their energy [8, 9]. In particular, it is this selectivity of fast-ion depletion or reorganization in velocity space that can be quantified with velocity-space tomography. Additionally, velocity-space tomography could be used to monitor phase-space engineering of fast-ion velocity distribution functions which has enabled control of sawteeth and of neoclassical tearing modes [10]. We show velocity-space tomographies using parameters typical for the ASDEX Upgrade collective Thomson scattering (CTS) [11–15] and fast-ion D_α (FIDA) diagnostics [16].

CTS and FIDA diagnostics are sensitive to 1D functions g of local fast-ion velocity distribution functions f in magnetically confined plasmas. The spatial resolution of the CTS diagnostic at ASDEX Upgrade is about 10 cm, and the measurement location can be moved freely in the plasma core by means of steerable antennas. The time resolution has often been set to 4 ms. CTS diagnostics are sensitive to the 1D projection of f onto the wave vector $\boldsymbol{k}^\delta = \boldsymbol{k}^s - \boldsymbol{k}^i$ which is the difference between the wave vectors of scattered radiation $\boldsymbol{k}^s$ and incident radiation $\boldsymbol{k}^i$. The most important angle to describe the pre-selected projection direction given by $\boldsymbol{k}^\delta$ is

the projection angle $\phi_{\mathrm{CTS}} = \angle(\boldsymbol{k}^{\delta}, \boldsymbol{B})$ where $\boldsymbol{B}$ is the magnetic field. In CTS experiments the ions leave spectral signatures in the scattered radiation. A frequency shift ν^{δ} of scattered radiation can be related to an ion velocity $\boldsymbol{v}$ projected onto $\boldsymbol{k}^{\delta}$:

$$\nu^{\delta} = \nu^{s} - \nu^{i} \approx \boldsymbol{v} \cdot \boldsymbol{k}^{\delta}/2\pi = uk^{\delta}/2\pi \tag{1}$$

where u is the projected velocity and $k^{\delta} = |\boldsymbol{k}^{\delta}|$. We define here a CTS *measurement* as detection of the fast-ion phase-space density in a particular interval in u that is related to an interval in ν^{δ} via equation (1). We define a *view* as a set of measurements taken in a projection direction described by ϕ_{CTS}. A second CTS receiver has been installed at ASDEX Upgrade in 2012, so that two simultaneous views with independently variable projection angles ϕ_{CTS} are available.

The location of a FIDA measurement is determined by the intersection of the injected neutral beam (NBI) and the line-of-sight (LOS) of the optical head. The spatial resolution of the FIDA diagnostic at ASDEX Upgrade is about 7 cm, and the time resolution is 2 ms. Beam source S3 is observed in the plasma core at two different fixed angles $\phi_{\mathrm{FIDA}} = \angle(\boldsymbol{k}^{\mathrm{LOS}}, \boldsymbol{B})$ where $\boldsymbol{k}^{\mathrm{LOS}}$ represents the wave vector along the LOS of the optical heads. The toroidal LOS has an angle of $\phi_{\mathrm{FIDA}} = 11^{\circ}$, and the new poloidal LOS has $\phi_{\mathrm{FIDA}} = 64^{\circ}$. The angles ϕ_{CTS} and ϕ_{FIDA} are analogue and will hereafter simply be called ϕ. FIDA diagnostics are also sensitive to 1D functions of f as the fast ions likewise leave a spectral signature in the detected light by Doppler shift and Stark splitting. For FIDA diagnostics no simple relation between the projected velocity u and the wavelength λ exists, so we define here as FIDA *measurement* the detection of Doppler- and Stark-shifted light in a particular wavelength interval.

Computed tomography in real space is used in many applications, for example in medical imaging in x-ray computed axial tomography (CAT or CT) scanners, positron emission tomography (PET) scanners or magnetic resonance imaging (MRI) scanners [17, 18]. It is also widely used in nuclear fusion research [19, 20]. We give a new prescription for tomographic reconstruction in velocity space that is analogue to those in real space. The prescription is based on CTS or FIDA weight functions [21–23] which were not available in previous work [24]. In [24] reconstructions from two and three synthetic CTS views have been shown to contain salient features of the underlying 2D fast-ion velocity distribution functions in idealized situations. It has since become conventional wisdom that a 2D velocity distribution function could not be found from one single 1D CTS or FIDA view and that at least two CTS or FIDA views with different projection directions would be necessary for that [12, 22–32]. We demonstrate that in fact just one single 1D CTS or FIDA view theoretically suffices to compute tomographies of almost the entire discrete 2D velocity distribution function under idealized conditions. Nevertheless, in simulated tokamak experiments with many CTS or FIDA views, the resemblance of tomographies and the original functions improves with the number of available views. Several tokamaks have been equipped with multiple FIDA views, for example DIII-D [33], NSTX [34], MAST or ASDEX Upgrade which is now also equipped with two CTS receivers. With our prescription we can compute tomographies for any set of fast-ion measurements, in particular those obtained with CTS or FIDA or other fast-ion charge exchange spectroscopy (FICXS) that detects other light than D_{α}. A mix of diagnostics would also be possible as will be relevant to the CTS/FIDA system at ASDEX Upgrade, the CTS/FICXS system at LHD [35, 36] and the proposed two-view CTS system for ITER [37–40] in particular if it can be combined with FICXS [32]. However, only one of the two CTS views is an enabled ITER diagnostic. One could also include neutral particle analysers (NPAs) or other fast-ion diagnostics in such mixes. We will study tomographies from such diagnostic mixes elsewhere.

In section 2 we will argue that one single 1D set of CTS measurements at different frequencies in fact theoretically suffices to reconstruct the original 2D velocity distribution function under ideal conditions. As weight functions form the core of our tomographic reconstruction prescription to be presented in section 4, we briefly review their meaning and use in section 3. Tomographic reconstructions of a variety of functions from synthetic CTS measurements under idealized conditions are demonstrated in section 5 and under simulated experimental conditions in section 6. In section 7 we show that tomographies can likewise be computed from synthetic FIDA measurements. We discuss the analogy of velocity-space tomography to real-space tomography in section 8 and draw conclusions in section 9.

2. Velocity-space tomography gedankenexperiment

First we perform a gedankenexperiment to motivate how one single 1D projection can in fact contain enough information to reconstruct the underlying 2D velocity-space distribution function in discrete problems. Suppose that Alice has a way to construct a 2D velocity-space distribution function f ion by ion and that Bob has a way to measure the 1D velocity distribution function g by CTS every time a new ion has been added. Bob will only know his own measurements obtained in a single CTS view. Alice adds an ion at some coordinate pair $(v_{\parallel}, v_{\perp})$ of her choice, for example at the location chosen in figure 1(*a*). Bob then measures g which would have the characteristic hammock shape shown in figure 1(*b*) [23, 41]. Bob can now work out the $(v_{\parallel}, v_{\perp})$-coordinates using

$$u = v_{\parallel} \cos\phi + v_{\perp} \sin\phi \cos\gamma, \tag{2}$$

where γ is the gyrophase of the ion [23]. Since $\cos\gamma$ takes values from -1 to 1, the width of the interval in which Bob detects the ion is $2v_{\perp} \sin\phi$. The centre of the interval is $v_{\parallel} \cos\phi$. Knowing his projection angle ϕ and the width and centre of his measured function g, he can tell at which coordinates $(v_{\parallel}, v_{\perp})$ Alice has added the ion. Alice then adds a second ion at a velocity-space location of her choice, and Bob again measures g by CTS. Now the function g looks more complicated but Bob can subtract his previous function g and has again a simple hammock-shaped function from which he can deduce the location of the second ion. This procedure can be repeated until the entire 2D velocity distribution function is constructed ion by ion, and Bob will know the entire function exactly, looking just at his 1D measurements. Alice could also construct f by adding collections of ions with identical velocities instead of single ions. Bob could then tell how many

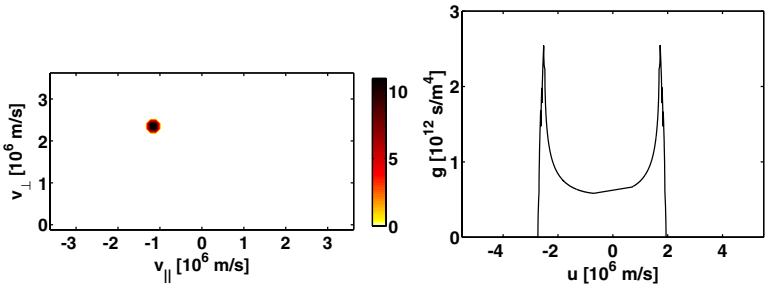

(a) f (b) g

Figure 1. (a) Example function f consisting of a single pixel in arbitrary units. (b) Projection g of the pixel function for a projection angle of $\phi = 70^\circ$.

ions have been added since the integral over u is proportional to the number of ions:

$$n = \int g \, \mathrm{d}u = \int\int f \, \mathrm{d}v_\parallel \, \mathrm{d}v_\perp. \tag{3}$$

This gedankenexperiment shows that one single 1D CTS view can in fact contain enough information for accurate reconstruction firstly in simple situations and secondly also in arbitrarily complicated situations if the complexity is added step by step. In real experiments only the complicated situation can be generated, and it is not immediately obvious that the 1D function g can contain enough information about the 2D function f. But we will demonstrate that we can compute accurate tomographies from one single CTS or FIDA view using our tomography reconstruction prescription if just enough information is available.

3. Discrete weight functions for CTS and FIDA

Discrete weight functions will lead to the tomographic reconstruction prescription presented in section 4. The reconstruction prescription in [24] did not use weight functions and was made tractable by expansion of the 1D (synthetic) measurements as well as the 2D fast-ion velocity distribution functions into orthonormal sets of base functions. Bessel functions have been used but other choices would be possible [24]. Exploiting CTS or FIDA weight functions [21–23] we will give a simpler reconstruction prescription that is inherently tractable and obviates the use of such expansions. Weight functions have previously been used in an alternative reconstruction prescription where the tomography was found by iteration. This has the disadvantage that the solution depends on the arbitrary start conditions of the iteration [23]. The new prescription we present gives unique solutions. In this section we define weight functions in discrete form.

Assuming f to be rotationally symmetric about the $v_\parallel$-axis, weight functions describe the mapping from 2D velocity-space distribution functions f to 1D functions g that are measured with CTS [23] or FIDA [22]. We here treat a discrete tomography problem and so also deal with discrete functions. The coordinates $(u, \phi, v_\parallel, v_\perp)$ are discretized in $(u_i, \phi_j, v_{\parallel k}, v_{\perp l})$ where the subscripts i, j, k, l run from 1 to the corresponding upper case letter I, J, K, L. I is the number of measurements at different u_i in a CTS or FIDA view, J is the number of available views, and (K, L) are the number of grid points in $(v_\parallel, v_\perp)$, respectively. $g_{ij} = g(u_i, \phi_j)$ is a matrix of discrete 1D functions in u_i for each viewing angle ϕ_j. $f_{kl} = f(v_{\parallel k}, v_{\perp l})$ is the discrete 2D velocity-space distribution function. g_{ij} and f_{kl} are related by discrete CTS or FIDA weight functions w_{ijkl} analogue to the continuous weight functions [23] so that

$$g_{ij} = \sum_{k=1}^{K} \sum_{l=1}^{L} w_{ijkl} f_{kl} \Delta v_\perp \Delta v_\parallel. \tag{4}$$

Weight functions pick out and assign weights to the velocity-space interrogation region that is observed for a particular projection angle ϕ_j and a projected velocity range at u_i (observed in a frequency range at f_i) for CTS or a wavelength range at λ_i for FIDA. In $(v_\parallel, v_\perp)$-coordinates CTS weight functions have a nearly triangular shape as shown in figure 2 for $u_i = 2 \times 10^6 \, \mathrm{m\,s^{-1}}$ and four typical projection angles ϕ_j. Weight functions describing CTS measurements quantify the probability that a gyrating ion with velocity $(v_\parallel, v_\perp)$ is observed in a particular projected velocity range at u_i for a given projection angle ϕ_j. The scattering must always originate from the coloured triangular region. A comprehensive discussion of weight functions for fast-ion CTS measurements is given elsewhere [23]. The weight functions describing FIDA measurements are more complicated and account for the charge exchange probability, the probability of photon emission from atomic level $n = 3$ to $n = 2$, Doppler shift of radiation originating from a gyrating particle, Stark splitting of the deuterium Balmer alpha line, and the instrument function of the FIDA spectrometer [16, 21, 22, 26, 29]. The Doppler shift part of FIDA weight functions is analogous to the CTS weight functions [23].

4. Tomographic reconstruction prescription

To find tomographies from CTS or FIDA measurements, we rewrite equation (4) to formulate a linear algebra problem of the form

$$W_{mn} F_n = G_m. \tag{5}$$

The matrix elements G_m, F_n and W_{mn} are, respectively, obtained from the matrix elements g_{ij}, f_{kl} and w_{ijkl} by

$$G_m = g_{ij} \tag{6}$$

$$F_n = f_{kl} \tag{7}$$

$$W_{mn} = w_{ijkl} \tag{8}$$

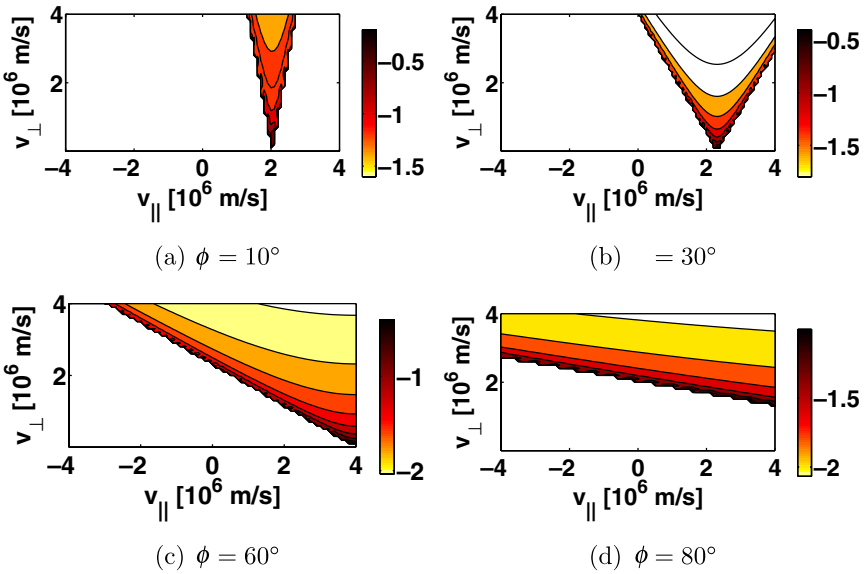

Figure 2. Gyromotion weight functions w for $u = 2 \times 10^6\,\mathrm{m\,s^{-1}}$ and various projection angles ϕ. The colourbar shows the base 10 logarithm.

using the assignment rules

$$m = (i-1) \times J + j \tag{9}$$

$$n = (k-1) \times L + l. \tag{10}$$

F is a column matrix of size $N \times 1$ obtained from the discrete 2D fast-ion velocity distribution function described by $N = K \times L$ points. G is a column matrix of size $M \times 1$ obtained from the discrete 1D functions measured with CTS or FIDA. If J views are available and I measurements in u_i (CTS) or λ_i (FIDA) are taken in each view, then the total number of measurements is $M = I \times J$. W is then a transfer matrix of size $M \times N$ taking F into G. The prescription given here corresponds to stacking lines or rows on top of each other but the order of this reorganization of the matrices is arbitrary as long as we obey equation (4). The forward problem to determine g from f or equivalently G from F is straightforward given that w and consequently W are known. An example of the action of the transfer matrix W on a pixel function F is illustrated in figure 1. The projection angle ϕ_j of this single-view example ($J = 1$) is set to 70°, and we compute a weight function for each u_i to obtain the value of G from the inner product WF. The 1D function G for a pixel function has the characteristic hammock shape shown in figure 1. The inverse problem to determine f from g or equivalently F from G is more complicated: we have to find an optimum solution F^+ to the under- or overdetermined system of linear equations (equation (5)) where W and G are known. We then also know f^+ because we know F^+ and the reorganization procedure.

We find an optimum solution to $WF = G$ for any size of W from the Moore–Penrose pseudoinverse or generalized inverse W^+ under positivity constraint. W^+ is a unique $N \times M$ matrix [42–44]. It can be computed from the singular value decomposition (SVD) of W: an $M \times N$ matrix W can always be decomposed uniquely as

$$W = U \Sigma V^{\mathrm{T}} \tag{11}$$

where U is the normalized eigenvector matrix of WW^{T} (an orthogonal $M \times M$ matrix), V is the normalized eigenvector matrix of $W^{\mathrm{T}}W$ (an orthogonal $N \times N$ matrix), V^{T} denotes the transpose of V, and Σ is a diagonal (but rectangular) $M \times N$ matrix [44]. The diagonal entries $\sigma_1, \sigma_2, ..., \sigma_R$ are the singular values of W, and R is the rank of W. The other entries of Σ are zero. The Moore–Penrose pseudoinverse is then

$$W^+ = V \Sigma^+ U^{\mathrm{T}} \tag{12}$$

Σ^+ is a diagonal (but also rectangular) $N \times M$ matrix, and the diagonal entries are $1/\sigma_1, 1/\sigma_2, ..., 1/\sigma_R$, i.e. the reciprocals of corresponding entries of Σ. The other entries of Σ^+ are zero. The computed tomography is then

$$F^+ = W^+ G. \tag{13}$$

This is the equation from which we could determine F^+ from actual measurements. If W is invertible, then W^+ is identical to the inverse W^{-1}. But W is generally a rectangular $M \times N$ matrix that cannot be inverted. If the system $WF = G$ is overdetermined, F^+ gives the minimum 2-norm of the residual $|WF - G|_2$. If the system $WF = G$ is underdetermined, F^+ is the particular solution with minimum 2-norm $|F|_2$ out of infinitely many solutions (the one with no nullspace component).

5. Tomographies under ideal conditions

In this section we firstly demonstrate that our prescription for computed tomography in velocity space can reproduce a variety of functions—any function we tested—in an idealized situation. Secondly, we also demonstrate that just one single synthetic CTS or FIDA view on that function suffices to construct an accurate tomography. We assume that the function can be described accurately on a numerical 2D grid, i.e. the grid size is so fine that even features on the smallest scale are accurately described. We also assume that there is no

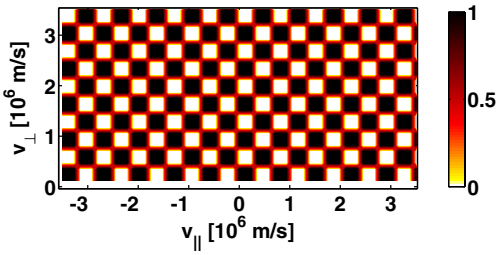

Figure 3. The original checkerboard function shown here is digitized in $N = 30 \times 61$ pixels. Typical 1D projections are shown in figure 4. Tomographies are shown in figure 5.

noise. The effects of insufficient resolution and noise will be discussed in section 6. Under these idealized conditions, we set the numerical grid of the tomography equal to that of the original function. As will be shown in section 6, these assumptions will not give a realistic picture of the recoverable information in real experiments. Nevertheless, previous work used identical grids for tomography and the original function [23, 24], and the results found in this section give an upper limit of the quality that can be achieved and demonstrate that one single view is enough under ideal conditions. Our prescription immediately suggests that the tomography should be very accurate in this case if just $M > N$ (more measurements than pixels). If the numerical grids of the original function and the tomography are equal, we can give a simple relation between F and F^+. One can substitute for G and use the orthogonality of U.

$$F^+ = W^+ G = W^+ W F = V \Sigma^+ U^{\mathrm{T}} U \Sigma V^{\mathrm{T}} F = V \Sigma^+ \Sigma V^{\mathrm{T}} F \tag{14}$$

$\Sigma^+\Sigma$ has as R ones on the diagonal and otherwise zeros. Therefore, only the first R columns and rows of V and V^{T} will be used in the reconstruction. In that sense the reconstruction for identical numerical grids is analogue to lossy data compression using SVD [44].

Under these assumptions, we reconstruct a checkerboard function (figure 3) and a pacman function (figure 6) using just one single view. We choose these test functions because it is easy to spot differences between the original function and the tomography. The checkerboard pattern in figure 3 covers the velocity-space region for $-3.5 \times 10^6\,\mathrm{m\,s^{-1}} < v_\parallel < 3.5 \times 10^6\,\mathrm{m\,s^{-1}}$ and $0 < v_\perp < 3.5 \times 10^6\,\mathrm{m\,s^{-1}}$ and is digitized in $N = 30 \times 61 = 1830$ pixels. This resolution is typical for simulated fast-ion velocity distribution functions today. We distribute M measurements evenly in the interval $-5 \times 10^6\,\mathrm{m\,s^{-1}} < u < 5 \times 10^6\,\mathrm{m\,s^{-1}}$ to ensure complete coverage of the velocity-space region we show here for any ϕ. Synthetic measurements in one single view for $\phi = 30^\circ$ and $M = 101$ to $M = 2501$ are illustrated in figure 4. By increasing the resolution one can capture an increasingly more fine-grained structure of g that contains recoverable information about the 2D function f. We stress that the noisy looking curve ($M = 2501$) is the accurate one whereas the smooth looking curve ($M = 101$) contains the least information. Actually the smooth curve has a large noise level originating from the discretization. The resolution in the u coordinate for $M = 101$ corresponds roughly to the resolution of most of the channels of the ASDEX Upgrade CTS receivers. Over 2500 measurements in one view seem possible in high-frequency resolution measurements that were demonstrated at TEXTOR [45–47].

Single-view tomographies computed from M synthetic measurements such as those in figure 4 are presented in figure 5. For any resolution they contain a fine-grained structure that is similar to that in the original in figure 3. Even for $M \sim N/20$ ($M = 101$), the tomography contains evenly distributed small-scale structures but they are larger than those in the original by a factor of two. The checkerboard pattern at a correct scale begins to emerge when $M \sim N/2$ ($M = 1001$). For $M \sim N$ the tomography closely resembles the original with minor defects, and for $M \sim 4N/3$ they are indistinguishable. The reconstruction prescription in previous work [24] failed to reconstruct the original function for low $v_\perp$ corresponding to about $v_\perp < 10^6\,\mathrm{m\,s^{-1}}$ in our graphs. The checkerboard patterns in figure 5 demonstrate that our prescription works for all $v_\perp$ about evenly.

Figure 7 shows single-view tomographies of the pacman function (figure 6), which we consider to be quite complex, for a various number of measurements M. From here on we do not use measurements in the interval $-0.7 \times 10^6 < u < 0.7 \times 10^6\,\mathrm{m\,s^{-1}}$. CTS due to bulk ions makes unambigous detection of fast ions very difficult if not impossible in this interval, and so we block it in the synthetic diagnostic. This loss of information results in the appearance of triangular regions that are not experimentally accessible (figures 7(*a*)–(*d*)). The shape of such triangles depends on the projection angle ϕ. The sides of these triangles are given by $v_\perp = (\mathrm{const} \times v_{\mathrm{th}} \pm v_\parallel \cos\phi)/\sin\phi$ and $v_\perp = 0$ [23]. The original pacman function contains complicated structures with a scale separation of one order of magnitude between the large-scale structures (pacman head, spook) and the small-scale fine details (eyes and mouth, zick zack pattern of the spook fringe). The tomography of the pacman function is also an accurate reproduction of the original function if M is large enough. The required number of measurements M for accurate tomographies is similar to the required M for the checkerboard—and in fact for any function we tested—and does not significantly depend on whether an interval in u has been blocked.

Lastly, we note that the projection angle ϕ is not very important in the idealized situation except for at $\phi = 90^\circ$ when all information about $v_\parallel$ is lost and at $\phi = 0^\circ$ where the weight functions are singular. No advantage is gained from having many views for an equal total number of measurements M in the idealized situation. For example a tomography from two views each with 1000 measurements ($M = 2 \times 1000 = 2000$) roughly resembles the original as much as the tomography from one view with $M = 2000$ measurements. Likewise, the angles are not important for many-view systems either if just the resolution of the measurements is high enough. The quality of the tomography for any number of views depends mostly on the total number of measurements M in the idealized situation.

6. Tomographies for heavily under-diagnosed fast-ion distribution functions

The previous section demonstrated that our tomography prescription will work in an idealized situation. The original function had the same number of grid points as

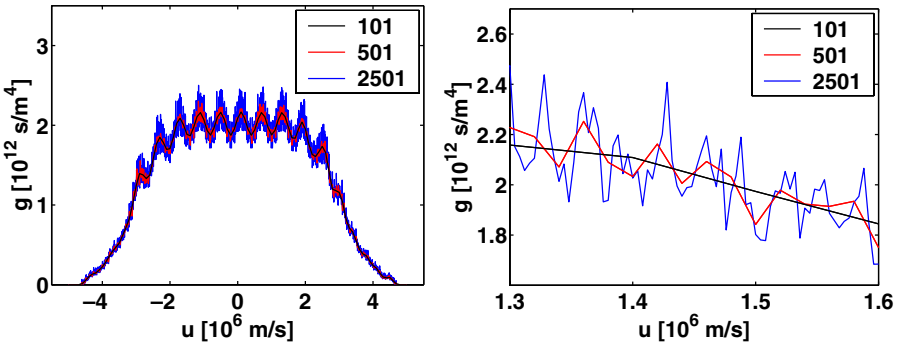

(a) (b)

Figure 4. Projections of the checkerboard function (figure 3) for $\phi = 30^\circ$ with $M = 101$, 501 and 2501 measurements in one view g. (*a*) Zoomed out showing the entire functions g. (*b*) Zoomed in showing that fine-scale structure can be resolved with $M = 2501$ measurements, which is sufficient to compute an accurate tomography.

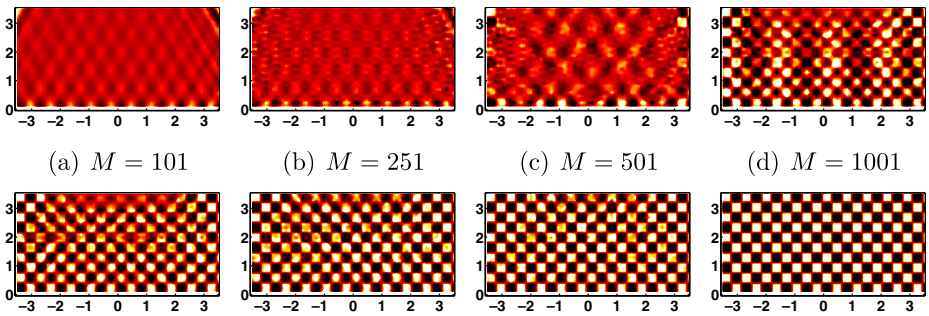

(a) $M = 101$ (b) $M = 251$ (c) $M = 501$ (d) $M = 1001$

(e) $M = 1251$ (f) $M = 1667$ (g) $M = 2001$ (h) $M = 2501$

Figure 5. Single-view tomographies of a checkerboard function in $N = 30 \times 61 = 1830$ pixels giving only M measurements at $\phi = 30^\circ$. The M measurements are evenly spaced in $-5 \times 10^6\,\mathrm{m\,s^{-1}} < u < 5 \times 10^6\,\mathrm{m\,s^{-1}}$. The number of measurements is varied from $M = 101$ to $M = 2501$. The axes and colourbars are identical to those for the original in figure 3.

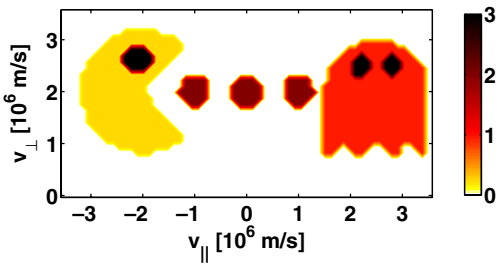

Figure 6. The original pacman function shown here is digitized in $N = 30 \times 61 = 1830$ pixels. Tomographies are shown in figure 7.

the reconstructions as in previous work [23, 24]. The 2D velocity distribution function in an actual tokamak experiment will have a fine-grained structure. It is then practically impossible to make enough CTS or FIDA measurements to carry all information about the fine-grained f. To simulate experimental conditions, we first construct a 1D projection g with M synthetic measurements from a finely resolved 2D distribution:

$$G = W_1 F. \tag{15}$$

Here we discretize f in $N_1 = 350 \times 701 \sim 250\,000$ grid points and take $M \sim 3400$ or $M \sim 340$ measurements leaving f under-diagnosed by a factor on the order of 100 or 1000, respectively. Accurate tomographies are impossible for such under-diagnosed f. Then we compute a tomography with a much lower number of grid points than N_1: $N_2 = 30 \times 61 = 1830 \ll N_1$.

$$F^+ = W_2^+ G. \tag{16}$$

Substitution of G now gives

$$F^+ = V_2 \Sigma_2^+ U_2^T W_1 F. \tag{17}$$

Substitution of the SVD of $W_1 = U_1 \Sigma_1 V_1^T$ does not lead to simplifications as in equation (14) since $U_2^T U_1$ does not disappear. If the grids for the tomography and the original function are not identical, it is necessary to truncate the SVD and use only singular values above a selected level. This is effectively also a lossy data compression technique since we find a lower rank approximation of the transfer matrix W_2 that has about rank $R \sim 1700$ in our example. Reference [24] used such a lossy data compression technique to simulate the effects of noise, noting that noise decreases the information content of the smallest singular values. The effect of noise and of under-diagnosing, i.e. computing the tomography on a much coarser grid than the original, are similar. $G = W_1 F$ is different from $G^+ = W_2 F^+$, and this difference can be interpreted as noise originating from the discretization.

Figure 8 shows a typical beam ion velocity distribution function at ASDEX Upgrade resolved on $N_1 = 350 \times 701$ grid points for which we present tomographies from CTS

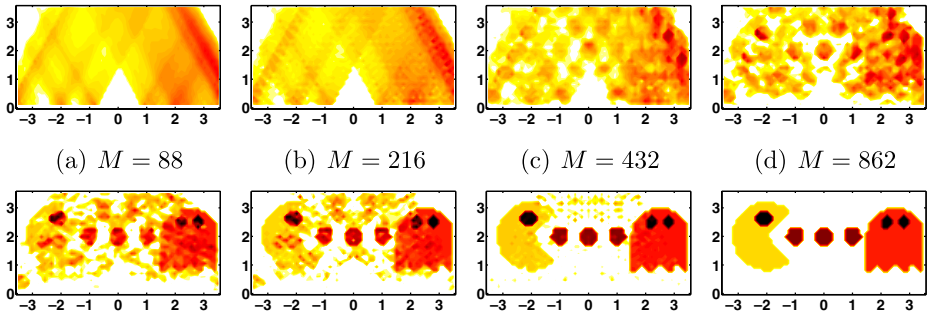

(a) $M = 88$ (b) $M = 216$ (c) $M = 432$ (d) $M = 862$

(e) $M = 1434$ (f) $M = 1722$ (g) $M = 2152$ (h) $M = 2868$

Figure 7. Single-view tomographies of a pacman function in 1830 pixels giving only M measurements at $\phi = 30°$. The M measurements are evenly spaced in $-5 \times 10^6\,\mathrm{m\,s^{-1}} < u < -0.7 \times 10^6\,\mathrm{m\,s^{-1}}$ and $0.7 \times 10^6\,\mathrm{m\,s^{-1}} < u < 5 \times 10^6\,\mathrm{m\,s^{-1}}$. The number of measurements is varied from $M = 88$ to $M = 2868$. The axes and colourbars are identical to those in figure 6.

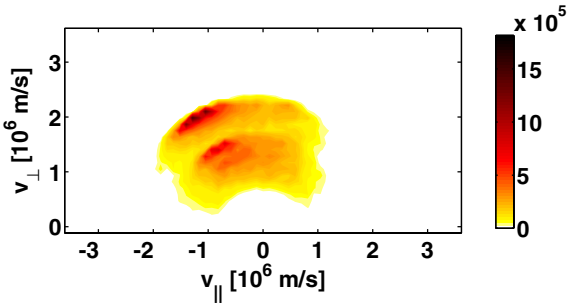

Figure 8. Typical beam ion distribution function for beam S3 at ASDEX Upgrade computed with TRANSP/NUBEAM. The distribution function is shown on a grid with 350 × 701 pixels.

measurements here. The original function has peaks at full and half injection energy of 60 keV in deuterium. We plot tomographies ($N_2 = 30 \times 61 = 1830$ grid points) of the original function in figure 9 for a various number of available views J and measurements M. The three-view and four-view CTS tomographies are proxies for mixed CTS/FIDA tomographies that can be reconstructed from the two available CTS views and the two available FIDA views at ASDEX Upgrade. The combination of different diagnostics in our method will be discussed elsewhere. We set the number of measurements per view inversely proportional to the number of views so that the total number of measurements M is almost the same in each column of figure 9. The left column shows tomographies for one to four views with about $M \sim 340$ measurements in total ($M < N$), and the right column with about $M \sim 3400$ measurements in total ($M > N$). In the idealized situation the number of views J is unimportant; only the number of measurements M matters. Therefore, just one view suffices for accurate tomographies in the idealized situation. However, under simulated experimental conditions, the number of views J is highly important for the relevance of the tomography to the original function. The single-view tomographies do not resemble the original function but they resemble rather the weight functions, and taking more measurements M in that one view does not help significantly. Nevertheless, the lopsidedness towards negative velocities is correctly reconstructed in the tomographies. For two views the region of the beam ions is roughly identifiable, and two maxima emerge. The four-view tomographies resemble the original function best. To quantify the difference between the original function and the tomography, we define an error measure as

$$Q_{\mathrm{tom}} = \frac{1}{n_{\mathrm{fast}}} \int\int |f - f^+|\,\mathrm{d}v_\parallel\,\mathrm{d}v_\perp \tag{18}$$

$$n_{\mathrm{fast}} = \int\int f\,\mathrm{d}v_\parallel\,\mathrm{d}v_\perp \tag{19}$$

which is a single number quantifying the resemblance of the tomography with the original function. $Q_{\mathrm{tom}} = 0$ means that the match is perfect, and $Q_{\mathrm{tom}} \sim 1$ means that f^+ does not resemble the original function f. In this example $Q_{\mathrm{tom}} = 1$ for one view, $Q_{\mathrm{tom}} = 0.8$ for two views, $Q_{\mathrm{tom}} = 0.7$ for three views and $Q_{\mathrm{tom}} = 0.5$ for four views, but the particular values depend on the particular distribution function and the diagnostic setup. This measure should be useful for future optimization studies. Comparing the low resolution column ($M < N$) with the high resolution column ($M > N$), we find that taking ten times more measurements per view does not help improving the tomographies much whereas adding extra views does. For the high resolution cases with $M \sim 3400$ only 340 singular values are useful whereas about 300 are useful in the low resolution cases with $M \sim 340$.

We now illustrate tomographies of a simpler function from synthetic CTS measurements. Figure 11 shows tomographies of a drifting Maxwellian function with $N_1 = 350 \times 701$ pixels (figure 10) that we then diagnose in one to four views, and we seek tomographies with $N_2 = 30 \times 61 = 1830$ pixels. Even though the number of measurements $M \sim 2000$ is again almost the same for the four cases, the tomographies improve with the number of views. One view is not enough to give tomographies that resemble the original. Nevertheless, the tomography for just one single view correctly identifies the location of the Maxwellian peak, so we can conclude that measurements in one single view contain relevant information about f even under simulated experimental conditions.

7. Tomographies from FIDA measurements

So far we have built the transfer matrix W from gyromotion weight functions, and these are sufficient to describe CTS measurements. Analytic expressions for these CTS weight functions are available [23]. Weight functions relevant to FIDA measurements are more complicated and are calculated

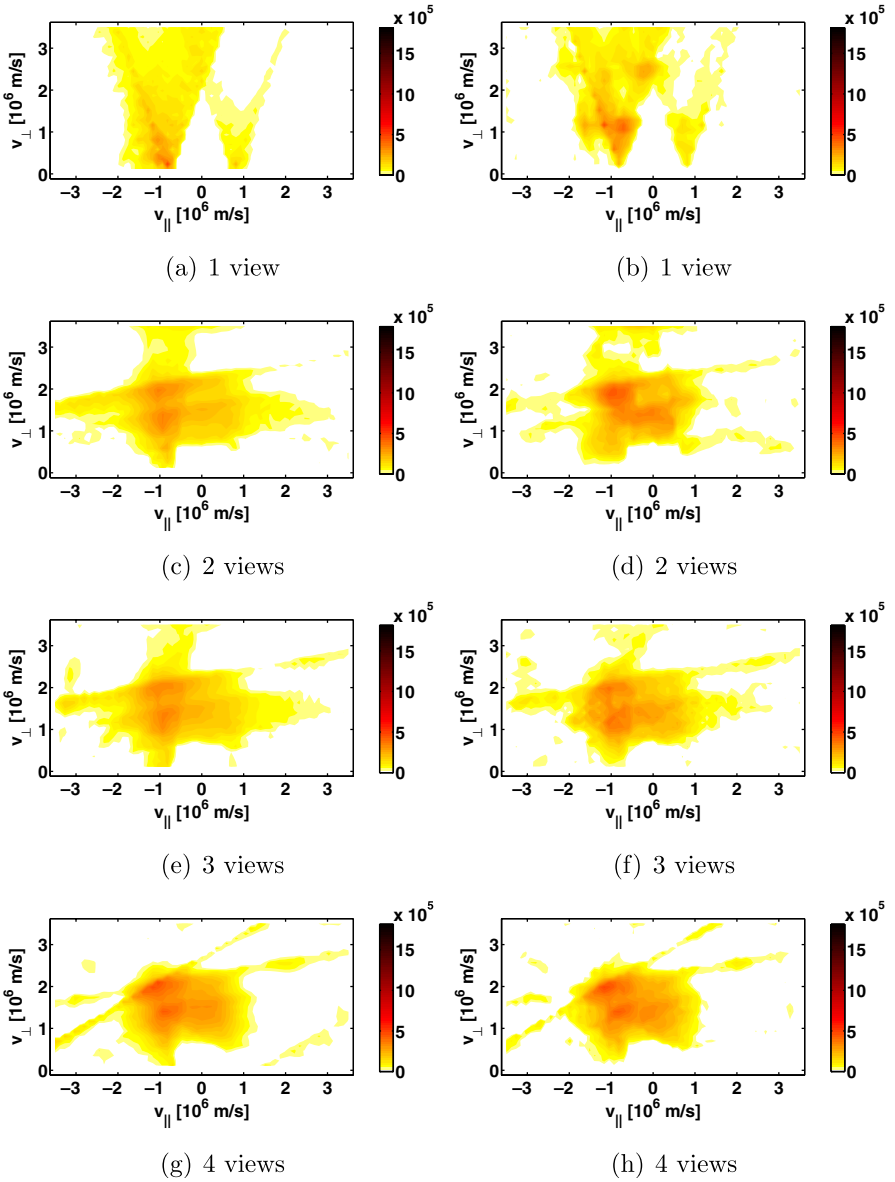

(a) 1 view (b) 1 view

(c) 2 views (d) 2 views

(e) 3 views (f) 3 views

(g) 4 views (h) 4 views

Figure 9. Tomographies ($N_2 = 30 \times 61$ pixels) of a typical beam ion distribution function ($N_1 = 350 \times 701$ pixels) for various numbers of views and measurements M. The total number of measurements M is similar in each column. In the left column (*a*), (*c*), (*e*), (*g*) $M \sim 340$ whereas in the right column (*b*), (*d*), (*f*), (*h*) $M \sim 3400$. The viewing angles are $\phi = 20^\circ$ for one view, $\phi = (10^\circ, 80^\circ)$ for two views, $\phi = (10^\circ, 40^\circ, 80^\circ)$ for three views and $\phi = (10^\circ, 30^\circ, 60^\circ, 80^\circ)$ for four views.

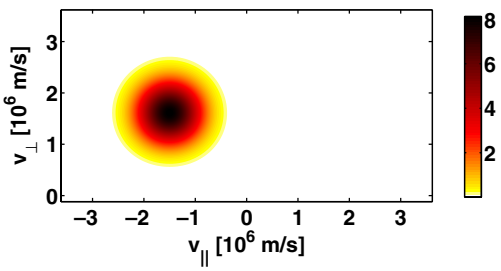

Figure 10. A drifting Maxwellian resolved in 350 × 701 pixels.

by counting photons in the different wavelength intervals. FIDA weight functions therefore contain numerical noise that decreases with the square root of the computer time allowed for their computation. We use $\phi = (11^\circ, 64^\circ)$ for the two FIDA views available at ASDEX Upgrade. The measurements M are evenly distributed in the wavelength intervals 649 nm $< \lambda <$ 654 nm and 659 nm $< \lambda <$ 663 nm. FIDA light cannot be observed in the wavelength interval 654 nm $< \lambda <$ 659 nm due to beam emission and halo neutrals [16], and so we exclude this wavelength range also in the synthetic measurements. Figure 12 shows a tomography of the original function (figure 8) from synthetic measurements for the two-view FIDA system at ASDEX Upgrade and demonstrates that our prescription also works for FIDA measurements. The original has $N_1 = 350 \times 701$ grid points which was here diagnosed by $M = 2 \times 90 = 180$ measurements, and the tomography in figure 12 has $N_2 = 30 \times 61 = 1830$ grid points. We here use the largest 80 singular values for the computation of the Moore–Penrose pseudoinverse.

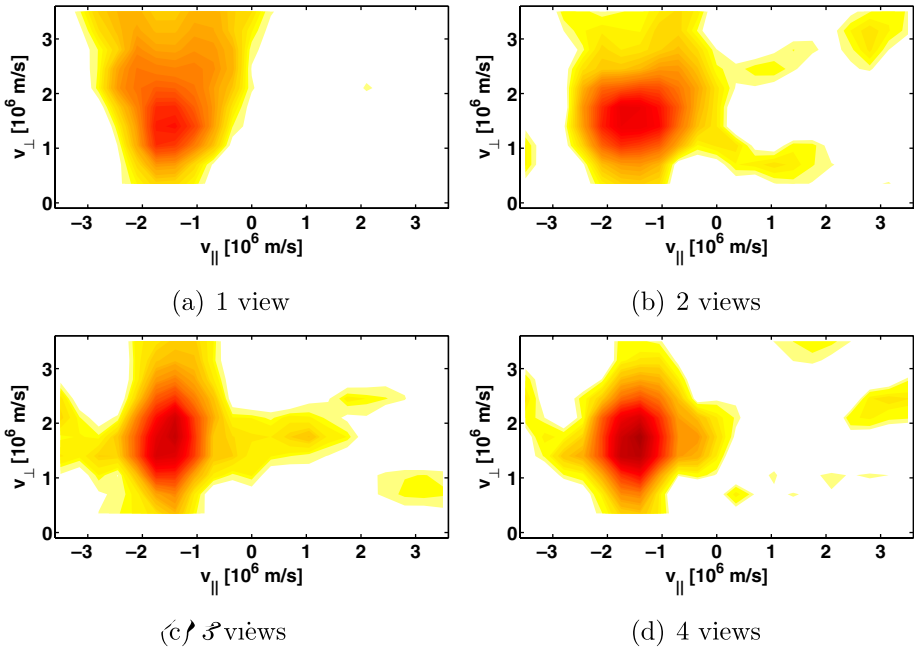

Figure 11. Tomographies in $N_2 = 30 \times 61 = 1830$ pixels for the drifting Maxwellian shown in figure 10 for $M \sim 2000$ evenly distributed on the available views. The viewing angles are $\phi = 20°$ for one view, $\phi = (30°, 60°)$ for two views, $\phi = (10°, 40°, 80°)$ for three views and $\phi = (10°, 30°, 60°, 80°)$ for four views.

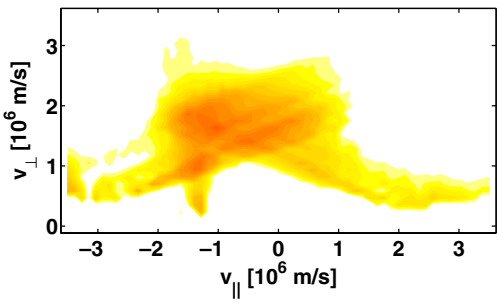

Figure 12. Tomography with $N_2 = 30 \times 61$ pixels from the two-view FIDA system with $\phi = (11°, 64°)$ and $M = 2 \times 90 = 180$ simulated measurements.

8. Analogy between real-space tomography and velocity-space tomography

Computed tomography in real space is a well-developed technique with applications in medical diagnostics, geo- and astrophysics, material science and many other disciplines [17, 18]. An important application is medical imaging in x-ray CT scanners, in MRI scanners, or in PET scanners. For example, x-ray CT scanners measure the absorption of several narrow x-ray beams through the patient. The absorption of x-rays depends on the tissue type, e.g. bones, muscle tissue, or fatty tissue. CT with x-rays may be carried out using a single x-ray source and a detector that are moved together to scan a beam through the patient. One viewing angle on the patient is not enough because the measurement is line-integrated and it is not known where along the LOS the x-rays have been absorbed. In CT scanners the source–detector arrangement is rotated, and the patient is scanned at another angle. By scanning the patient at many angles one can deduce a tomography of absorption coefficients that in turn give the tissue type. We note that tomographies in medical imaging thankfully operate with overdetermined systems of equations to obtain their accurate results.

It would be misleading to identify the FIDA or CTS projection angle ϕ with the viewing angle of the rotating apparatus of medical CT scanners. In plasmas in fact we have an intrinsic rotation of the object that allows a multitude of measurements: the gyration of the ions about the magnetic field. This gyration allows measurements of an ion at different frequency shifts via equations (1) and (2). It is this multitude of frequency-space measurements in velocity-space tomography that is analogue to the different viewing angles in real-space tomography. Many viewing angles in velocity space improve tomographies under realistic conditions but they are not essential under idealized conditions. For that reason one single CTS or FIDA view suffices for a tomography of the velocity-space distribution function in an idealized situation if just the resolution of the frequency-space measurements is high enough.

9. Conclusions

We have presented a new prescription for tomographic reconstruction of 2D fast-ion velocity distribution functions from CTS and FIDA measurements. By computing tomographies from synthetic measurements, we have demonstrated our prescription to give accurate tomographies of arbitrary functions in an idealized situation, and we have shown promise and limits of its application to real experiments. Our tomographic and theoretical results contradict the conventional wisdom that at least two CTS or FIDA views would necessarily be required for tomography of fast-ion velocity distribution functions [12, 22–32]. In an idealized situation in fact just one single CTS or FIDA view suffices to compute an accurate

tomography. Under simulated experimental conditions, tomographies contain salient features of the original fast-ion velocity distribution function showing that 2D information can be recovered from the 1D measurements in one single view. The lopsidedness of a beam ion velocity distribution and the peak location of a drifting Maxwellian function can correctly be reproduced in single-view tomographies for a range of angles but otherwise single-view tomographies do not resemble the original functions. For many-view systems the resemblance of the tomography and the original improves each time a new CTS or FIDA view is added, even if the resolution is varied inversely proportional to the number of views so that the total number of measurements in all views is constant. For a four-view system, the tomography of a realistic beam ion velocity distribution function at ASDEX Upgrade resembles the original function well in general shape and location of the beam injection sources at full and half energies. By applying our prescription to a set of real CTS or FIDA measurements with many views, one could determine a tomography of the 2D fast-ion velocity distribution function experimentally.

Acknowledgments

This work, supported by the European Communities under the contract of Association between Euratom and DTU was partly carried out within the framework of the European Fusion Development Agreement. The views and opinions expressed herein do not necessarily reflect those of the European Commission.

References

[1] Nielsen S.K. *et al* 2010 Fast-ion redistribution due to sawtooth crash in the TEXTOR tokamak measured by collective Thomson scattering *Plasma Phys. Control. Fusion* **52** 092001

[2] Nielsen S.K. *et al* 2011 Dynamics of fast ions during sawtooth oscillations in the TEXTOR tokamak measured by collective Thomson scattering *Nucl. Fusion* **51** 063014

[3] Muscatello C.M., Heidbrink W.W., Kolesnichenko Ya.I., Lutsenko V.V., Van Zeeland M.A. and Yakovenko Yu.V. 2012 Velocity-space studies of fast-ion transport at a sawtooth crash in neutral-beam heated plasmas *Plasma Phys. Control. Fusion* **54** 025006

[4] Garcia-Munoz M. *et al* 2011 Fast-ion transport induced by Alfvén eigenmodes in the ASDEX Upgrade tokamak *Nucl. Fusion* **51** 103013

[5] Van Zeeland M.A. *et al* 2011 Measurements and modeling of Alfvén eigenmode induced fast ion transport and loss in DIII-D and ASDEX Upgrade *Phys. Plasmas* **18** 056114

[6] Pace D.C., Fisher R.K., García-Muñoz M., Heidbrink W.W. and Van Zeeland M.A. 2011 Convective beam ion losses due to Alfvén eigenmodes in DIII-D reversed-shear plasmas *Plasma Phys. Control. Fusion* **53** 062001

[7] García-Muñoz M., Martin P., Fahrbach H.-U., Gobbin M., Günter S., Maraschek M., Marrelli L., Zohm H. and the ASDEX Upgrade Team 2007 NTM induced fast ion losses in ASDEX Upgrade *Nucl. Fusion* **47** L10–5

[8] Hauff T., Pueschel M., Dannert T. and Jenko F. 2009 Electrostatic and magnetic transport of energetic ions in turbulent plasmas *Phys. Rev. Lett.* **102** 075004

[9] Heidbrink W., Park J., Murakami M., Petty C., Holcomb C. and Van Zeeland M. 2009 Evidence for fast-ion transport by microturbulence *Phys. Rev. Lett.* **103** 175001

[10] Graves J.P., ChapmanI.T., Coda S., Lennholm M., Albergante M. and Jucker M. 2012 Control of magnetohydrodynamic stability by phase space engineering of energetic ions in tokamak plasmas *Nature Commun.* **3** 624

[11] Meo F. *et al* 2008 Commissioning activities and first results from the collective Thomson scattering diagnostic on ASDEX Upgrade (invited) *Rev. Sci. Instrum.* **79** 10E501

[12] Salewski M. *et al* 2010 Comparison of fast ion collective Thomson scattering measurements at ASDEX Upgrade with numerical simulations *Nucl. Fusion.* **50** 035012

[13] Meo F. *et al* and The Asdex Upgrade Team 2010 First results and analysis of collective Thomson scattering (CTS) fast ion distribution measurements on ASDEX Upgrade *J. Phys.: Conf. Ser.* **227** 012010

[14] Furtula V., Salewski M., Leipold F., Michelsen P.K., Korsholm S.B., Meo F., Moseev D., Nielsen S.K., Stejner M. and Johansen T. 2012 Design and performance of the collective Thomson scattering receiver at ASDEX Upgrade *Rev. Sci. Instrum.* **83** 013507

[15] Furtula V., Leipold F., Salewski M., Michelsen P.K., Korsholm S.B., Meo F., Moseev D., Nielsen S.K., Stejner M. and Johansen T. 2012 Performance measurements of the collective Thomson scattering receiver at ASDEX Upgrade *J. Instrum.* **7** C02039

[16] Geiger B., Garcia-Munoz M., Heidbrink W.W., McDermott R.M., Tardini G., Dux R., Fischer R. and Igochine V. 2011 Fast-ion D-alpha measurements at ASDEX Upgrade *Plasma Phys. Control. Fusion* **53** 065010

[17] Kak A.C. and Slaney M. 1998 *Principles of Computerized Tomographic Imaging* (New York: IEEE Press)

[18] Herman G.T. 2009 *Fundamentals of Computerized Tomography* 2nd edn (Berlin: Springer)

[19] Anton M., Weisen H., Dutch M.J., von der Linden W., Buhlmann F., Chavan R., Marletaz B., Marmillod P. and Paris P. 1996 X-ray tomography on the TCV tokamak *Plasma Phys. Control. Fusion* **38** 1849–78

[20] Ingesson L.C., Alper B., Chen H., Edwards A.W., Fehmers G.C., Fuchs J.C., Giannella R., Gill R.D., Lauro-Taroni L. and Romanelli M. 1998 Soft x ray tomography during ELMs and impurity injection in JET *Nucl. Fusion* **38** 1675–94

[21] Heidbrink W.W., Luo Y., Burrell K.H., Harvey R.W., Pinsker R.I. and Ruskov E. 2007 Measurements of fast-ion acceleration at cyclotron harmonics using Balmer-alpha spectroscopy *Plasma Phys. Control. Fusion* **49** 1457–75

[22] Heidbrink W.W. 2010 Fast-ion Dα measurements of the fast-ion distribution (invited) *Rev. Sci. Instrum.* **81** 10D727

[23] Salewski M. *et al* 2011 On velocity space interrogation regions of fast-ion collective Thomson scattering at ITER *Nucl. Fusion* **51** 083014

[24] Egedal J. and Bindslev H. 2004 Reconstruction of gyrotropic phase-space distributions from one-dimensional projections *Phys. Plasmas* **11** 2191

[25] Heidbrink W.W., Bell R.E., Luo Y. and Solomon W. 2006 Fast-ion D-alpha diagnostic for NSTX *Rev. Sci. Instrum.* **77** 10F120

[26] Luo Y., Heidbrink W.W., Burrell K.H., Kaplan D.H. and Gohil P. 2007 Measurement of the D alpha spectrum produced by fast ions in DIII-D *Rev. Sci. Instrum.* **78** 033505

[27] Luo Y., Heidbrink W.W., Burrell K.H., Ruskov E. and Solomon W.M. 2007 Fast-ion D_α measurements and simulations in quiet plasmas *Phys. Plasmas* **14** 112503

[28] Podestà M., Heidbrink W.W., Bell R.E. and Feder R. 2008 The NSTX fast-ion D-alpha diagnostic *Rev. Sci. Instrum.* **79** 10E521

[29] Van Zeeland M.A., Heidbrink W.W. and Yu J.H. 2009 Fast ion D α imaging in the DIII-D tokamak *Plasma Phys. Control. Fusion* **51** 055001

[30] Van Zeeland M.A. 2010 Imaging key aspects of fast ion physics in the DIII-D tokamak *Nucl. Fusion* **50** 084002

[31] Heidbrink W.W., Liu D., Luo Y., Ruskov E. and Geiger B. 2011 A code that simulates fast-ion D(alpha) and neutral particle measurements *Commun. Comput. Phys.* **10** 716–41
[32] Kappatou A., Delabie E., Jaspers R.J.E. and von Hellermann M.G. 2012 Feasibility of non-thermal helium measurements with charge exchange spectroscopy on ITER *Nucl. Fusion* **52** 043007
[33] Muscatello C.M., Heidbrink W.W., Taussig D. and Burrell K.H. 2010 Extended fast-ion D-alpha diagnostic on DIII-D *Rev. Sci. Instrum.* **81** 10D316
[34] Bortolon A., Heidbrink W.W. and Podestà M. 2010 A tangentially viewing fast ion D-alpha diagnostic for NSTX *Rev. Sci. Instrum.* **81** 10D728
[35] Kubo S. *et al* 2010 Collective Thomson scattering of a high power electron cyclotron resonance heating beam in LHD (invited) *Rev. Sci. Instrum.* **81** 10D535
[36] Ito T., Osakabe M., Ida K., Yoshinuma M., Kobayashi M., Murakami S., Goto M., Takeiri Y., Reiter D. and Okamura S. 2012 Effect of halo neutrals on fast-ion charge exchange spectroscopy measurements in LHD *Plasma Fusion Res.* **5** S2099
[37] Salewski M., Meo F., Bindslev H., Furtula V., Korsholm S.B., Lauritzen B., Leipold F., Michelsen P.K., Nielsen S.K. and Nonbøl E. 2008 Investigation of first mirror heating for the collective Thomson scattering diagnostic in ITER *Rev. Sci. Instrum.* **79** 10E729
[38] Salewski M. *et al* 2009 Comparison of collective Thomson scattering signals due to fast ions in ITER scenarios with fusion and auxiliary heating *Plasma Phys. Control. Fusion* **51** 035006
[39] Salewski M., Eriksson L.-G., Bindslev H., Korsholm S.B., Leipold F., Meo F., Michelsen P.K. and Nielsen S.K. 2009 Impact of ICRH on the measuritent of fusion alphas by collective Thomson scattering in ITER *Nucl. Fusion* **49** 025006
[40] Leipold F., Furtula V., Salewski M., Bindslev H., Korsholm S.B., Meo F., Michelsen P.K., Moseev D., Nielsen S.K. and Stejner M. 2009 Antenna design for fast ion collective Thomson scattering diagnostic for the international thermonuclear experimental reactor *Rev. Sci. Instrum.* **80** 093501
[41] Heidbrink W.W., Burrell K.H., Luo Y., Pablant N.A. and Ruskov E. 2004 Hydrogenic fast-ion diagnostic using Balmer-alpha light *Plasma Phys. Control. Fusion* **46** 1855–75
[42] Moore E.H. 1920 The fourteenth western meeting of the American Mathematical Society *Bull. Am. Math. Soc.* **26** 385–96
[43] Penrose R. 1955 A generalized inverse for matrices *Math. Pro. Camb. Phil. Soc.* **51** 406–13
[44] Strang G. 1988 *Linear Algebra and its Applications* (Orlando, FL: Harcourth Brace Jovanovich)
[45] Stejner M. *et al* 2010 Collective Thomson scattering measurements with high frequency resolution at TEXTOR *Rev. Sci. Instrum.* **81** 10D515
[46] Korsholm S.B. *et al* 2011 Measurements of intrinsic ion Bernstein waves in tokamak by collective Thomson scattering *Phys. Rev. Lett.* **106** 165004
[47] Stejner M. *et al* 2012 Measurements of plasma composition in the TEXTOR tokamak by collective Thomson scattering *Plasma Phys. Control. Fusion* **54** 015008